

EPIC 216747137: a new HW Vir eclipsing binary with a massive sdOB primary and a low-mass M-dwarf companion

R. Silvotti,^{1*} V. Schaffenroth,² U. Heber,³ R. H. Østensen,⁴ J. H. Telting,⁵ J. Vos,² D. Kilkenny,⁶ L. Mancini,^{7,8,1} S. Ciceri,⁹ A. Irrgang,³ H. Drechsel³

¹INAF-Osservatorio Astrofisico di Torino, Strada dell'Osservatorio 20, 10025 Pino Torinese, Italy

²University of Potsdam, Institute of Physics and Astronomy, Karl-Liebknecht-Str. 24-25, 14476 Potsdam, Germany

³Dr. Remeis-Sternwarte & ECAP, Astronomical Institute, University of Erlangen-Nürnberg, Sternwartstr. 7, 96049 Bamberg, Germany

⁴Department of Physics, Astronomy and Materials Science, Missouri State University, 901 S. National, Springfield, MO 65897, USA

⁵Nordic Optical Telescope, Rambla José Ana Fernández Pérez 7, 38711 Breña Baja, Spain

⁶Department of Physics & Astronomy, University of the Western Cape, Private Bag X17, Bellville 7535, South Africa

⁷Department of Physics, University of Rome “Tor Vergata”, Via della Ricerca Scientifica 1, 00133 Roma, Italy

⁸Max Planck Institute for Astronomy, Königstuhl 17, 69117 Heidelberg, Germany

⁹simona.ciceri@gmail.com (Last Institution: Department of Astronomy, Stockholm University, Stockholm, Sweden)

Accepted 2020 October 18. Received 2020 October 16; in original form 2020 October 1

ABSTRACT

EPIC 216747137 is a new HW Virginis system discovered by the *Kepler* spacecraft during its *K2* “second life”. Like the other HW Vir systems, EPIC 216747137 is a post-common-envelope eclipsing binary consisting of a hot subluminescent star and a cool low-mass companion. The short orbital period of 3.87 hours produces a strong reflection effect from the secondary ($\sim 9\%$ in the R band). Together with AA Dor and V1828 Aql, EPIC 216747137 belongs to a small subgroup of HW Vir systems with a hot evolved sdOB primary. We find the following atmospheric parameters for the hot component: $T_{\text{eff}} = 40400 \pm 1000$ K, $\log g = 5.56 \pm 0.06$, $\log(N(\text{He})/N(\text{H})) = -2.59 \pm 0.05$. The sdOB rotational velocity $v \sin i = 51 \pm 10$ km s⁻¹ implies that the stellar rotation is slower than the orbital revolution and the system is not synchronized. When we combine photometric and spectroscopic results with the Gaia parallax, the best solution for the system corresponds to a primary with a mass of about 0.62 M_{\odot} close to, and likely beyond, the central helium exhaustion, while the cool M-dwarf companion has a mass of about 0.11 M_{\odot} .

Key words: stars: horizontal branch; stars: binaries: eclipsing; stars: individual: EPIC 216747137.

1 INTRODUCTION

Post-common-envelope binaries (PCEBs) are crucial to study the poorly understood and short-lived common-envelope phase of stellar evolution.

Among PCEBs, HW Virginis stars are a specific class of eclipsing binaries consisting of a hot subdwarf primary with an M-dwarf companion (see Heber 2016 for a recent review on hot subdwarf stars). There are two subgroups of HW Vir stars: those similar to the prototype, with a core-helium-burning sdB (subdwarf B) primary, located in the extreme horizontal branch (EHB) part of the H-R diagram. And those like AA Dor, with a hotter and more evolved pri-

mary of sdOB spectral class, beyond the central helium exhaustion.

The possibility of measuring accurate dynamical masses in HW Virginis systems is important to shed light on the formation mechanism of hot subdwarfs. These stars are characterized by very thin hydrogen envelopes and masses close to the canonical mass of 0.47 M_{\odot} .

To form such an object, the hydrogen envelope of the red giant progenitor must be removed almost completely. Han et al. (2002, 2003, see also Clausen et al. 2012) describe three main binary evolution scenarios to form an sdB star: (i) common envelope (CE) ejection, (ii) stable Roche-lobe overflow (RLOF), and (iii) the merger of two He white dwarfs. The latter scenario may contribute only for a very small fraction of sdBs given that the high masses and high rotation rates foreseen are not supported by the observa-

* E-mail: roberto.silvotti@inaf.it

tions (Fontaine et al. 2012; Charpinet et al. 2018; Reed et al. 2018). Since $\sim 50\%$ of the non-composite-spectrum hot subdwarfs are members of short-period binaries with orbital periods between 0.027 and ~ 30 days (Maxted et al. 2001; Napiwotzki et al. 2004; Kupfer et al. 2015, 2020), mostly with a white dwarf (WD) or an M-type main-sequence (MS) companion, CE ejection triggered by a close companion is generally regarded as the main formation channel. As far as the RLOF scenario is concerned, an important recent work by Pelisoli et al. (2020) shows that almost all the wide binaries with K to F-type MS companions that they analysed show evidence of previous interaction, confirming that the RLOF is another efficient way to form $\sim 30\text{--}40\%$ of hot subdwarfs, and suggesting that binary interaction may *always* be required to form a hot subdwarf star. Indeed, Stark & Wade (2003) found that $\sim 40\%$ of hot subdwarfs have colors consistent with the presence of an unresolved late-type companion in a magnitude-limited sample (or $\sim 30\%$ in a volume-limited sample). Putting these numbers together, we can estimate that $\sim 35\%$ of hot subdwarfs are in close binaries with M-dwarf or WD companions, while $\sim 30\%$ are in wide binaries with F/G/K companions.

However, the remaining fraction of $\sim 35\%$ consists of apparently single hot subdwarfs. For them, different formation mechanisms have been invoked, including the merger of a He white dwarf with a low-mass hydrogen-burning star (Clausen & Wade 2011). The presence of a substellar companion, difficult to detect, orbiting the sdB progenitor is another possibility (Soker 1998; Han et al. 2012), only partially supported by the observations.

On the one hand, no planets transiting hot subdwarfs were found in a large survey with the Evryscope, capable of detecting planets with radii slightly smaller than Jupiter (Ratzloff et al. 2020). Neither were planetary transits of hot subdwarfs found up to now by the Kepler/K2 or the TESS space missions. Moreover, no significant radial velocity (RV) variations were found from high-accuracy Harps-N measurements of a small sample of 8 bright apparently single sdB stars (Silvotti et al. 2020), excluding the presence of close substellar companions down to a few Jupiter masses and, for half of these stars, excluding also the presence of higher-mass companions in wide orbits. These null results do not exclude that the planets were completely destroyed during the CE phase or that their envelope was removed leaving a very small and dense planetary core, difficult to detect (see e.g. the controversial cases of KIC 5807616 and KIC 10001893, Charpinet et al. 2011; Silvotti et al. 2014).

On the other hand, there are at least three known HW-Vir systems with brown dwarf (BD) companions having masses between 0.04 and 0.07 M_{\odot} (Geier et al. 2011; Schaffferroth et al. 2014, 2015), plus two more with masses close to the hydrogen-burning limit (Schaffferroth et al. 2019, Fig. 14 and 15). And there are a few controversial cases of planet detections through the eclipse or pulsation timing method (see e.g. Baran et al. 2016 and references therein).

Thanks to the high number of new HW-Vir systems discovered recently from the light curves of the OGLE and ATLAS projects (Schaffferroth et al. 2019), and the new ones that are being discovered by the TESS mission, the number of HW-Vir systems with substellar companions is likely to grow significantly in the short term. With enough statistics it should be possible to determine the minimum mass for

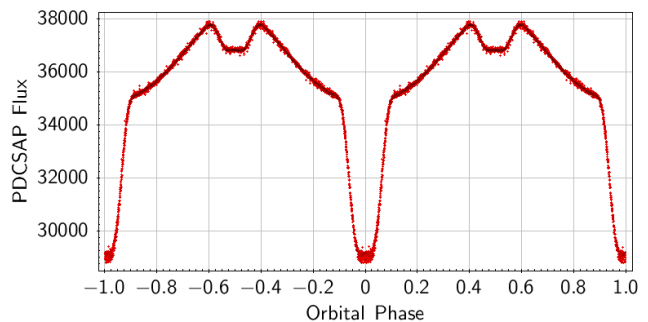


Figure 1. K2 light curve.

a substellar companion to eject the red giant envelope and survive engulfment. According to theory, it was thought that this limit could be near $10 M_{\text{Jup}}$ (Soker 1998; Han et al. 2012), but a recent article suggests that this mass limit could be higher, around $30\text{--}50 M_{\text{Jup}}$ (Kramer et al. 2020).

The system described in this paper, EPIC 216747137 (alias UCAC2 23234937), is a new HW-Vir binary relatively bright (Gaia DR2 magnitude $G = 13.767 \pm 0.004$), located about 880 pc from us (Gaia DR2 parallax of 1.14 ± 0.06 mas). In the next sections we present the results of an analysis of both photometric and spectroscopic data of EPIC 216747137, that allow us to infer the orbital parameters of the system and the main characteristics of the primary and secondary components.

2 TIME-SERIES PHOTOMETRY

2.1 K2 discovery

EPIC 216747137 was observed by the *Kepler* space telescope during cycle 7 of its K2 secondary mission in long-cadence mode, with a sampling time of 29.42 minutes. We downloaded the data from the “Barbara A. Mikulski Archive for Space Telescopes” (MAST)¹ and we used the PDCSAP fluxes (PDC=Presearch Data Conditioning, SAP=Simple Aperture Photometry, see K2 documentation for more details). After having removed some bad data point (those with SAP_QUALITY flag different from zero or 2048 plus two outliers), the data set we used, as shown in Fig. 1, consists of 81.3 days from BJD_{TBD} 2457301.48620 to 2457382.80453 (corresponding to 05/10/2015 – 26/12/2015).

2.2 SAAO BVR data

EPIC 216747137 was re-observed at the Sutherland site of the South African Astronomical Observatory (SAAO) using the 1-m Elizabeth telescope with the STE3 CCD photometer which has a read-out time of about 6 s (pre-binned 2×2), small compared to the exposure times for filters B (60 s), V (30 s) and R (30 s). Observations were made using each filter on a separate night (18, 17 and 19 May 2017, respectively) to maximise the resolution of the light curve. Reduction of the CCD frames, magnitude extraction by profile-fitting, and differential correction using several

¹ archive.stsci.edu

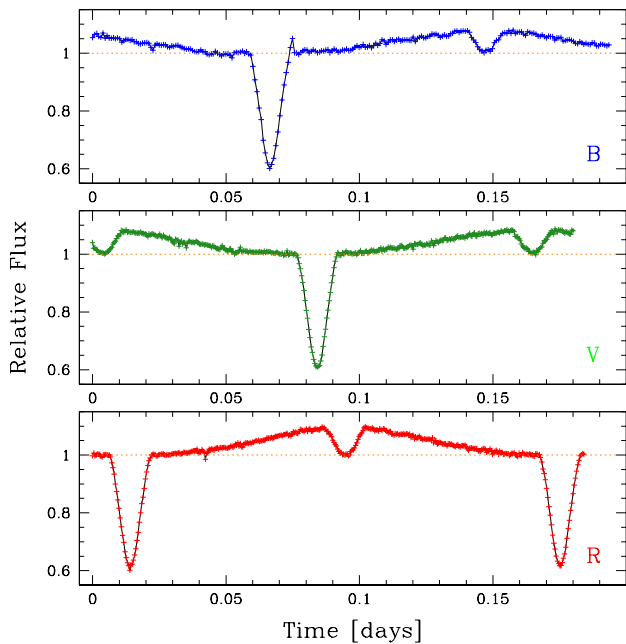


Figure 2. SAAO BVR light curves. The flux is normalized to the level just before and just after the primary eclipse.

field stars were performed using software written by Darragh O’Donoghue and partly based on the DoPHOT program described by Schechter et al. (1993).

The BVR light curves are shown in Fig. 2. Comparing Fig. 1 with Fig. 2, we immediately note the different shape and depth of the primary and secondary eclipses, due to the smearing caused by the poor sampling rate of the *K2* long-cadence data. In Fig. 1 the primary and secondary eclipse have a depth of $\sim 17\%$ and less than 3% respectively, while they are much deeper in the SAAO data ($\sim 39\%$ and $\sim 8\%$ in the R band). For this reason, the *K2* data was used only to improve the ephemeris, while the analysis of the light curve was performed using the ground-based photometry.

3 RADIAL VELOCITIES

EPIC 216747137 was observed spectroscopically with various instruments. As a first step, in order to measure the radial velocities (RVs) of the primary, 9 high-resolution spectra were obtained at different orbital phases in July and September 2016 using FEROS with the 2.2 m MPG/ESO telescope at La Silla Observatory in Chile, with exposure times of 1800 s^2 . The FEROS spectra were reduced using CERES, a pipeline written for échelle spectrographs described in Brahm et al. (2017). The raw spectra were first corrected with calibration frames obtained in the afternoon or during twilight, and then calibrated in wavelength using a Th-Ar spectrum. The radial velocities of the sdOB star were measured from the He II line at 4686 \AA , while the Balmer lines were not used because they give more noisy results. However, the results were quite poor due to the low SN ratio of the FEROS spectra.

² For the first two spectra we used 1000 and 1500 s.

For this reason, new observations were carried out as part of our *K2* sdBV follow-up spectroscopic survey (Telting et al. 2014). We obtained 32 low-resolution spectra ($R\sim 2000$, or 2.2 \AA) in two runs (22 spectra in July 2017, 10 spectra between March and August 2018) at the 2.56 m Nordic Optical Telescope (NOT, La Palma) using ALFOSC, 600 s exposure times, grism#18, 0.5 arcsec slit, and CCD#14, giving an approximate wavelength range 345–535 nm. The spectra were homogeneously reduced and analysed. Standard reduction steps within IRAF include bias subtraction, removal of pixel-to-pixel sensitivity variations, optimal spectral extraction, and wavelength calibration based on helium arc-lamp spectra. The peak signal-to-noise ratio of the individual spectra ranges from 50 to 125. The RVs were measured using the lines $H\beta$, $H\gamma$, $H\delta$, $H8$ and $H9$ through a cross-correlation analysis in which we used as a template a synthetic fit to an orbit-corrected average (all spectra shifted to zero velocity before averaging).

Finally, 32 medium-resolution spectra were obtained with MagE@Magellan I at Las Campanas Observatory in Chile in 3.5 hours on September 17, 2017, with 300 s exposure times, 1 arcsec slit, $R\sim 4100$ and a useful wavelength range of $3500\text{--}8100\text{ \AA}$. The typical signal-to-noise ratios were between 80 and 110. The spectra were reduced using the MagE pipeline (Kelson et al. 2000; Kelson 2003). The RVs were measured using Balmer lines and two He I lines at 4471 and 5875 \AA .

The RV measurements obtained from the MagE spectra are the most accurate due to the best compromise between high SN ratio, relatively high resolution and short exposure times, which means lower smearing. However, the ALFOSC and FEROS RVs were also used using appropriate weights (Fig. 3). From the best RV fit we obtain a circular orbit with a RV amplitude $K=52.3\pm 1.3\text{ km/s}$, and a system velocity $v_0=-6.4\pm 1.2\text{ km/s}$. Smearing is not considered as it is negligible for MagE and ALFOSC spectra (0.08% and 0.3% respectively) and has little importance only for FEROS spectra (3%). By fitting all the 73 RVs listed in Table 1 with an eccentric solution, we can constrain the eccentricity to a value smaller than 0.091^3 .

Both the ALFOSC and MagE spectra were used not only to measure the radial velocities, but also to derive accurate atmospheric parameters and the rotational velocity of the sdOB star and to measure their variations as a function of the orbital phase, as described in the next section.

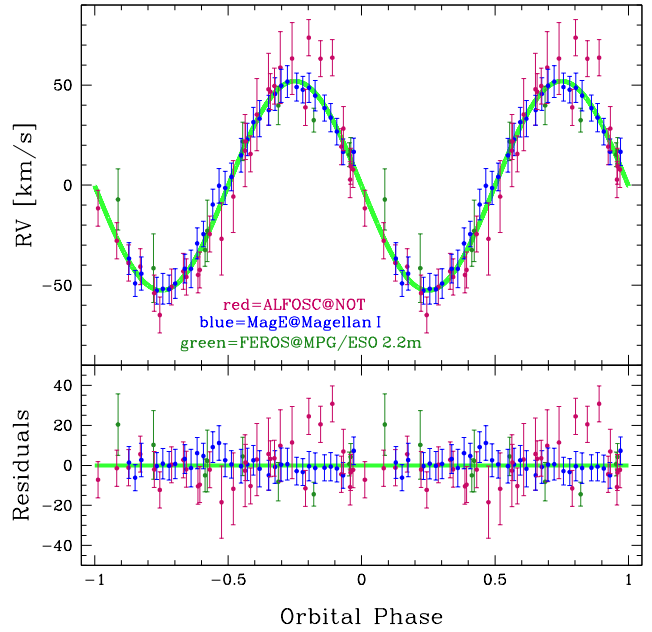
4 ATMOSPHERIC PARAMETERS AND ROTATIONAL VELOCITY OF THE PRIMARY

The reflection effect adds additional light to the sdOB spectrum, which varies with phase. Because we can not model this contribution, each individual spectrum is matched separately to a grid of synthetic models to derive the effective temperature, gravity and helium abundance. If the contribution to the spectrum of the primary is significant, the resulting atmospheric parameters should show trends with orbital phase as a consequence of the varying light pollution.

³ We obtain an eccentricity of 0.019 ± 0.024 , which translates into a 3σ upper limit of 0.091.

Table 1. RV measurements.

BJD _{TDB} -2450000.	RV [km/s]	error [km/s]	instr.	UT date
7590.682242	11.14	6.64	FEROS	2016-07-21
7590.755434	-38.47	8.18	FEROS	2016-07-21
7645.521343	-28.90	15.42	FEROS	2016-09-14
7645.542780	15.74	9.59	FEROS	2016-09-14
7645.564206	33.73	9.60	FEROS	2016-09-14
7645.585628	26.38	6.00	FEROS	2016-09-14
7645.607066	9.17	6.00	FEROS	2016-09-14
7645.628503	-13.21	15.33	FEROS	2016-09-14
7645.649944	-47.56	17.09	FEROS	2016-09-14
7958.472032	-51.96	9.00	ALFOSC	2017-07-23
7958.479132	-50.91	9.00	ALFOSC	2017-07-23
7958.486222	-30.49	9.00	ALFOSC	2017-07-23
7958.493322	-32.92	18.00	ALFOSC	2017-07-23
7958.500422	-11.79	18.00	ALFOSC	2017-07-24
7958.507522	11.19	18.00	ALFOSC	2017-07-24
7958.514612	29.18	18.00	ALFOSC	2017-07-24
7958.521712	41.84	18.00	ALFOSC	2017-07-24
7958.528812	52.66	18.00	ALFOSC	2017-07-24
7958.535902	57.18	18.00	ALFOSC	2017-07-24
7958.565612	13.15	9.00	ALFOSC	2017-07-24
7958.572712	1.74	9.00	ALFOSC	2017-07-24
7958.579812	-17.64	9.00	ALFOSC	2017-07-24
7958.591172	-33.85	9.00	ALFOSC	2017-07-24
7958.598262	-44.95	9.00	ALFOSC	2017-07-24
7958.605362	-46.79	9.00	ALFOSC	2017-07-24
7960.478821	67.59	9.00	ALFOSC	2017-07-25
7960.485921	57.11	9.00	ALFOSC	2017-07-25
7960.493021	57.61	9.00	ALFOSC	2017-07-25
7960.549991	-70.95	9.00	ALFOSC	2017-07-26
7960.557091	-56.91	9.00	ALFOSC	2017-07-26
7960.564181	-49.15	9.00	ALFOSC	2017-07-26
8014.490569	-42.73	7.92	MagE	2017-09-17
8014.494309	-55.17	6.49	MagE	2017-09-17
8014.498039	-50.28	8.30	MagE	2017-09-17
8014.507289	-58.76	6.72	MagE	2017-09-18
8014.511029	-57.84	7.66	MagE	2017-09-18
8014.514759	-58.11	7.13	MagE	2017-09-18
8014.518489	-55.26	7.36	MagE	2017-09-18
8014.524279	-47.81	7.19	MagE	2017-09-18
8014.528019	-47.87	9.37	MagE	2017-09-18
8014.531749	-35.15	7.80	MagE	2017-09-18
8014.535489	-30.53	6.37	MagE	2017-09-18
8014.541189	-15.77	7.71	MagE	2017-09-18
8014.544929	-6.39	8.64	MagE	2017-09-18
8014.548659	-7.49	8.26	MagE	2017-09-18
8014.552399	-1.96	6.91	MagE	2017-09-18
8014.558219	8.82	8.43	MagE	2017-09-18
8014.561949	16.75	8.10	MagE	2017-09-18
8014.565679	25.39	7.44	MagE	2017-09-18
8014.569419	27.14	9.01	MagE	2017-09-18
8014.574989	31.38	7.49	MagE	2017-09-18
8014.578729	39.47	8.14	MagE	2017-09-18
8014.582469	43.56	8.29	MagE	2017-09-18
8014.586199	45.64	7.96	MagE	2017-09-18
8014.591779	42.95	6.97	MagE	2017-09-18
8014.595519	41.63	6.68	MagE	2017-09-18
8014.599249	42.56	7.36	MagE	2017-09-18
8014.602999	38.63	7.62	MagE	2017-09-18
8014.608619	32.41	6.52	MagE	2017-09-18
8014.612359	27.67	7.08	MagE	2017-09-18
8014.616089	20.70	6.67	MagE	2017-09-18
8014.619829	10.60	6.42	MagE	2017-09-18

**Figure 3.** Radial velocities.**Table 1 – continued**

BJD _{TDB} -2450000.	RV [km/s]	error [km/s]	instr.	UT date
8014.626199	10.55	6.89	MagE	2017-09-18
8201.763003	32.78	9.00	ALFOSC	2018-03-24
8211.685742	-48.44	9.00	ALFOSC	2018-04-03
8268.635281	3.39	9.00	ALFOSC	2018-05-30
8269.702361	9.53	9.00	ALFOSC	2018-05-31
8304.505900	40.62	9.00	ALFOSC	2018-07-05
8304.596910	-60.01	9.00	ALFOSC	2018-07-05
8307.568760	43.45	9.00	ALFOSC	2018-07-08
8312.607699	-3.29	9.00	ALFOSC	2018-07-13
8338.477179	15.78	9.00	ALFOSC	2018-08-07
8338.536299	22.17	11.10	ALFOSC	2018-08-08

Indeed, such apparent variations of atmospheric parameters have been found in other reflection binaries such as HW Vir (Wood & Saffer 1999), HS 0705+6700 (Drechsel et al. 2001) and most distinctively in HS 2333+3937 (Heber et al. 2004). The best estimate of the atmospheric parameters comes from data taken during secondary eclipse and just before and after primary eclipse, when the light pollution should be lowest.

We closely follow the analysis strategy outlined by Heber et al. (2004). The Balmer and helium lines in the ALFOSC and MagE spectra are used to determine effective temperature, gravity and helium abundance, and the projected rotation velocity $v \sin i$. Because the spectral resolution of the ALFOSC spectra is insufficient for $v \sin i$ to be determined, the latter is derived from the MagE spectra. The ALFOSC spectra show the entire Balmer series with a well defined continuum and can, therefore, be used to determine T_{eff} , $\log g$ and $\log y = \log(N(\text{He})/N(\text{H}))$. For the MagE spectra, their wavy run of the continuum prohibits the Balmer lines to be used. However, they are very useful

to derive the projected rotation velocity and allow us to investigate the helium ionisation equilibrium including lines not covered by the ALFOSC spectral range, from which an independent estimate of the effective temperature can be obtained. Since the helium lines are quite insensitive to gravity, the gravity had to be fixed in the analysis of the MagE spectra to $\log g = 5.56$ derived from the ALFOSC spectra. We match the Balmer ($H\beta$ to $H11$) and He I (4471 and 4026 Å), as well as He II 4686 and 4542 Å line profiles in the ALFOSC spectra, and He I (4471 and 5875 Å) and He II (4686 and 5411 Å) lines in the MagE spectra with a grid of synthetic spectra.

The models are computed using three codes. First, the ATLAS12 code (Kurucz 1996) is used to compute the atmospheric structure (temperature/density stratification) in LTE. Non-LTE population numbers are then calculated with the DETAIL code (Giddings 1981) and the coupled equations of radiative transfer and statistical equilibrium are solved numerically. In the final step, the SURFACE code (Giddings 1981) computes the emergent spectrum based on the non-LTE occupation numbers provided by DETAIL. In this step detailed line-broadening tables are incorporated. All three codes have been updated recently (see Irrgang et al. 2018). The impact of departures from LTE for hydrogen and helium on the atmospheric structure is modelled by feeding back population numbers calculated by DETAIL to ATLAS12 and iterate. In addition, the occupation probability formalism (Hubeny et al. 1994) for hydrogen has been implemented and line broadening tables have been updated. Stark broadening tables for hydrogen and neutral helium are taken from Tremblay & Bergeron (2009) and Beauchamp et al. (1997), respectively. The broadening of the lines of ionised helium was treated as described by Auer & Mihalas (1972).

The observed spectra are matched to the model grid by χ^2 minimisation as described by Saffer et al. (1994) using implementations by Napiwotzki et al. (1999) and Hirsch (2009). Exemplary fits to an ALFOSC and a MagE spectrum are shown in Fig. 4 and Fig. 5.

The results of the quantitative spectral analysis of all ALFOSC and MagE spectra are summarized in Fig. 6. In the left panels (ALFOSC), the apparent variations of the effective temperature with phase and an amplitude of ~ 2500 K are obvious. The lowest temperatures (~ 40 kK) occur near primary eclipse and in the secondary eclipse, where the contribution by extra light should be minimal. Hence, the increase during other orbital phases is caused by reflected light and, therefore, not real. Similarly, variations of the helium abundance are observed. The apparent variations of the surface gravity, however, are small. The mean values adopted for T_{eff} , $\log g$ and $\log y$, summarized in Table 2, are obtained by selecting six spectra close to the primary eclipse with phase between -0.1 and $+0.1$ and adding one spectrum at phase 0.52. The analysis of the MagE spectra also results in effective temperatures and helium abundances that seem to vary with orbital phase (cf. Fig. 6 right panels), but with amplitudes less pronounced than those from the ALFOSC spectra. For this reason, we use all the MagE spectra to compute mean values and standard deviations of T_{eff} and $\log y$ (cf. Table 2).

The effective temperature and surface gravity of EPIC 216747137 ($T_{\text{eff}} = 40400$ K and $\log g = 5.56$) are very similar to the hot HW Vir systems AA Dor (Klepp & Rauch

Table 2. SdOB atmospheric parameters and rotational velocity

	ALFOSC	MagE	Adopted
T_{eff} (K)	39800 ± 400	41000 ± 400	40400 ± 1000
$\log g$ (cgs)	5.56 ± 0.04		5.56 ± 0.06
$\log y$	$-2.58_{-0.18}^{+0.13}$	$-2.59_{-0.05}^{+0.04}$	-2.59 ± 0.05
$v \sin i$ (km/s)		51 ± 10	51 ± 10

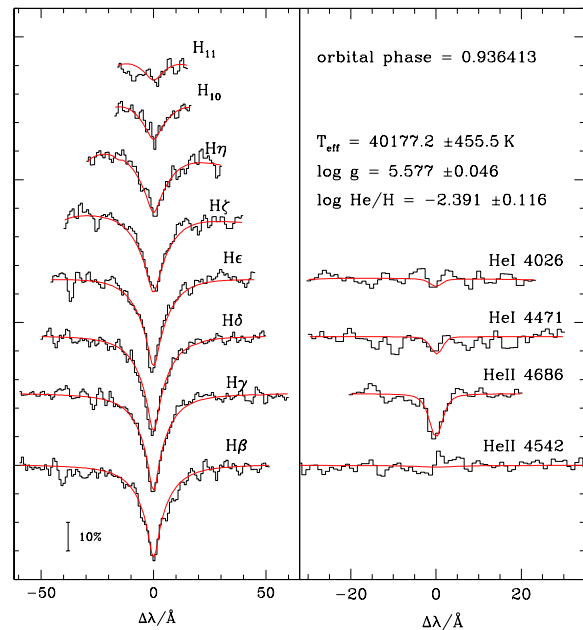


Figure 4. Fit of one of the ALFOSC spectra corresponding to orbital phase 0.9364, close to the primary eclipse, for which the contribution of the secondary is minimum.

2011) and V1828 Aql (= NSVS 14256825, Almeida et al. 2012). EPIC 216747137 also shares an underabundance of helium ($\log y = -2.59$) with the two others.

The projected rotational velocity, as derived from the individual MagE spectra (central right panel of Fig. 6), results in a mean $v \sin i = 51 \pm 10$ km s $^{-1}$, significantly less than ~ 70 km s $^{-1}$ expected for tidally locked rotation. Mean rotational velocity of 51 km s $^{-1}$ and standard deviation of 10 km s $^{-1}$ are obtained excluding only a single outlier close to phase 0 (see central right panel of Fig. 6).

5 STELLAR PARAMETERS: RADIUS, MASS, AND LUMINOSITY

The second data release of Gaia provided a precise (5%) parallax measurement which allows the stellar parameters (radius, mass, and luminosity) to be derived from the atmospheric parameters, if the angular diameter were known. The latter can be derived from the spectral energy distribution (SED).

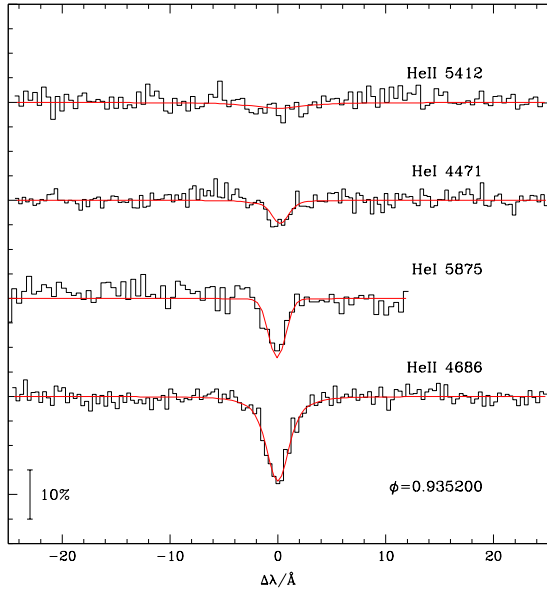


Figure 5. Same as Fig. 4 but for one of the MagE spectra corresponding to orbital phase 0.9352.

5.1 Angular diameter and interstellar reddening

The angular diameter Θ is derived from the observed flux $f(\lambda)$ and the synthetic stellar surface flux via the relation $f(\lambda) = \Theta^2 F(\lambda)/4$, which means that Θ is just a scaling factor which shifts fluxes up and down. Strictly speaking, the apparent magnitudes of the sdOB can be measured during secondary eclipses only, when the companion is completely eclipsed by the larger subdwarf, because of the contamination by light from the companion’s heated hemisphere. Such data are not available. Nevertheless, many photometric measurements are available in different filter systems, covering the spectral range in the optical and infrared. However, those measurements are mostly averages of observations taken at multiple epochs and, therefore, may be subject to light pollution from the companion.

The low Galactic latitude ($b = -9.9^\circ$) implies that interstellar reddening may be large. Therefore the angular diameter has to be determined along with the interstellar colour excess. The reddening law of Fitzpatrick et al. (2019) and a synthetic flux distribution from the grid of model atmospheres described in Sect. 4 is matched to the observed magnitudes employing a χ^2 based fitting routine (see Heber et al. 2018 for details). The final atmospheric parameters and their respective uncertainties derived from the quantitative spectral analysis (see Sect. 4) are used. Indeed, interstellar reddening is significant with $E(B-V) = 0.213^{+0.010}_{-0.016}$ mag (see Table 3). The latter is consistent with values from reddening maps of Schlegel et al. (1998) and Schlafly & Finkbeiner (2011): 0.253 mag and 0.217 mag, respectively.

Because of light pollution from the companion’s heated hemisphere, the resulting angular diameter will be somewhat overestimated, as that is not accounted for in the synthetic SED. Red and infrared magnitudes are expected to be more affected than the blue ones. To account for the additional light, we added a black-body spectrum to the fit, allowing

Table 3. SED + Gaia DR2 results

Atmospheric parameters from spectral analysis	
Effective temperature T_{eff}	40400 ± 1000 K
Surface gravity $\log(g(\text{cm s}^{-2}))$	5.56 ± 0.06
Helium abundance $\log y$	-2.59 ± 0.05
Parameters from SED fit & Gaia DR2 parallax	
Color excess $E(B - V)$	$0.213^{+0.010}_{-0.016}$ mag
Metallicity z (fixed)	0 dex
Angular diameter $\log(\Theta(\text{rad}))$	$-10.975^{+0.009}_{-0.015}$
Black-body temperature T_{bb}	2900^{+2600}_{-1300} K
Black-body surface ratio $A_{eff,bb}/A_{eff}$	$2.5^{+4.3}_{-1.4}$
Generic excess noise δ_{excess} (fixed)	0.033 mag
Parallax ϖ (RUWE=1.04, offset=0.029 mas)*	1.14 ± 0.06 mas
$R = \Theta/(2\varpi)$	$0.206 \pm 0.012 R_\odot$
$M = gR^2/G$	$0.56^{+0.11}_{-0.10} M_\odot$
$L/L_\odot = (R/R_\odot)^2 (T_{\text{eff}}/T_{\text{eff},\odot})^4$	$100^{+16}_{-15} L_\odot$

* We use the RUWE parameter as a quality indicator, best is 1, <1.4 is acceptable, 1.04 is good.

its temperature as well as the relative emission area to vary. The final fit is shown in Fig. 7 and results summarized in Table 3.

5.2 Stellar radius, mass and luminosity

The Gaia DR2 parallax is corrected for a zero-point offset of -0.029 mas as recommended by Lindgren et al. (2018) and applied by Bailer-Jones et al. (2018) to derive distances. By combining it with the atmospheric parameters ($\log g$ and T_{eff}) and the angular diameter, we can determine the star’s radius R , mass M , and luminosity L . The respective uncertainties of the stellar parameters are derived by Monte Carlo error propagation. Results are summarized in Table 3. Once the radius ($R = 0.206 \pm 0.012 R_\odot$) has been derived from angular diameter and parallax, the mass ($0.56^{+0.11}_{-0.10} M_\odot$) follows from gravity and the luminosity ($100^{+16}_{-15} L_\odot$) from radius and effective temperature.

A comparison with evolutionary models for EHB stars by Han et al. (2002) is shown in Fig. 8 and demonstrates that the hot subdwarf has likely just evolved beyond the core-helium-burning phase, similar to AA Dor (Klepp & Rauch 2011) and V1828 Aql (Almeida et al. 2012), or is at the very end of helium burning, depending on the hot subdwarf mass and envelope mass.

6 EPHEMERIS

First we computed independent ephemerides from photometric and RV data, obtaining a good agreement on the orbital period. The orbital period derived from the RVs has a higher precision thanks to the longer baseline (2.0 vs 1.6 years) and also because of the poor time resolution of the $K2$ data. Then, considering both spectroscopic and photometric data together, we were able to remove the degeneracy due to the spectral windows and obtain a better determination of the orbital period thanks to the longer baseline (2.8 yrs). In practice, taking as reference the center of the primary

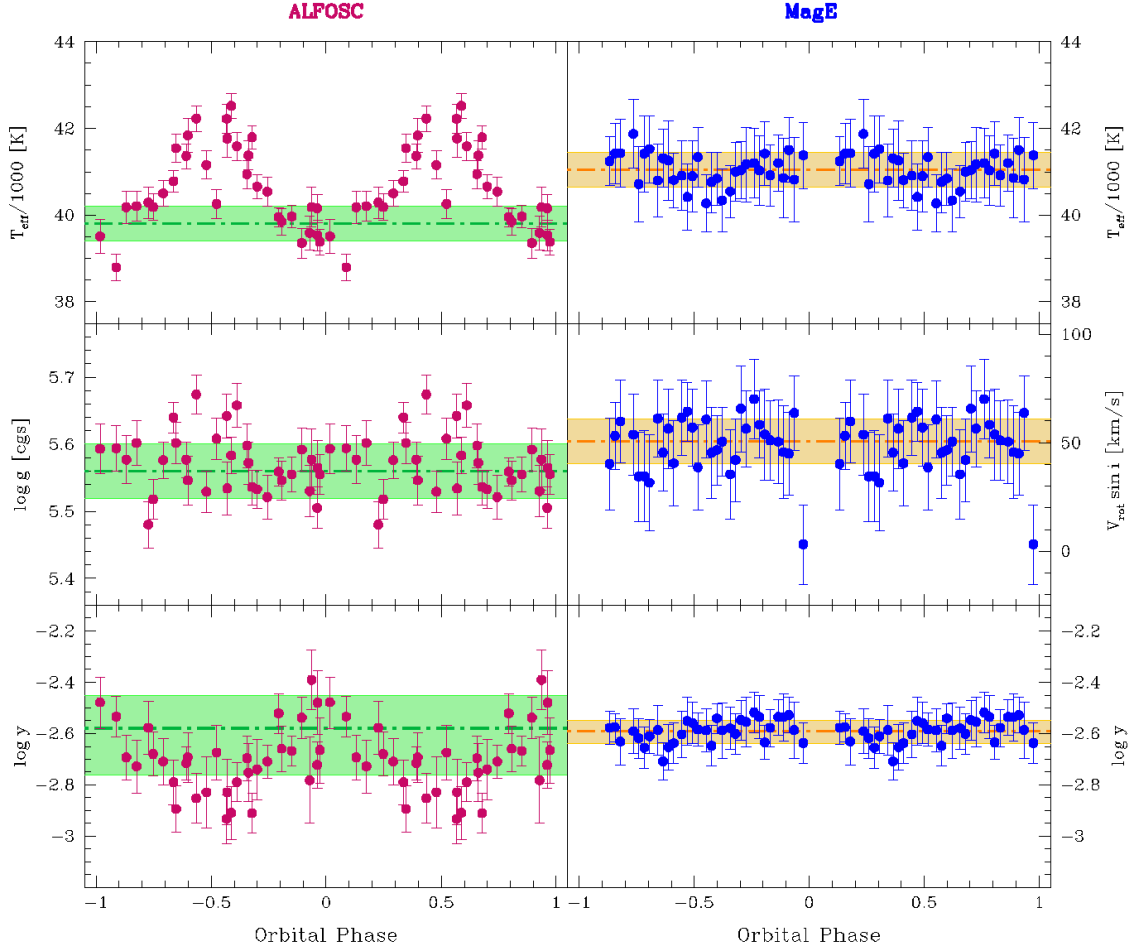


Figure 6. T_{eff} , $\log g$, $\log y$ and $v_{\text{rot}} \sin i$ variations as a function of the orbital phase. Left panels: ALFOSC. The green dotted-dashed horizontal lines mark the adopted T_{eff} , $\log g$, and $\log y$ and the associated errors (cf. Table 2 and text). Note the two points with low T_{eff} near phase 0.5 (secondary eclipse), when the contribution of the secondary is strongly reduced. Right panels: MagE. The orange dotted-dashed horizontal lines mark the average values and associated errors of T_{eff} , $v_{\text{rot}} \sin i$, and He abundance. In the central panel note the outlier near phase zero (primary eclipse).

eclipse, we verified that the time difference between the last primary eclipse of our data set (determined from RVs) and the first one (determined from photometry) was very close to an integer multiple of the orbital period determined from the RVs. Then, imposing that such time difference is *exactly* a multiple of the orbital period, we obtain the best determination of the orbital period and the following best ephemeris:

$$\text{BJD}_{TDB} = (2457301.56346 \pm 0.00041) + (0.16107224 \pm 0.00000017) E$$

where BJD_{TDB} is the barycentric Julian date of the center of each primary eclipse using barycentric dynamical time (see e.g. Eastman et al. 2010).

7 MODELING OF THE LIGHT CURVE

The SAAO BRV light curves show relatively deep eclipses together with a reflection effect with increasing amplitude from B to R, and a secondary eclipse only visible due to the reflection effect. Such a light curve is characteristic for sdO/B systems with close, cool, low-mass companions. For

the modeling of the light curve we used LCURVE, a code written to model detached but also accreting binaries containing a white dwarf (for details, see Copperwheat et al. 2010). It has been used to analyse several detached white dwarf-M dwarf binaries (e.g., Parsons et al. 2010), which show very similar light curves with deep eclipses and a prominent reflection effect, if the primary is a hot white dwarf. Recently, LCURVE was used also for an sdB+BD system (Schafferoth et al. 2020, submitted). The code subdivides each star into small elements with a geometry fixed by its radius as measured along the direction towards the other star. Roche distortions and irradiation are also included, as well as limb-darkening, gravitational darkening, lensing, Doppler beaming, Rømer delay and asynchronous orbits. The latter three effects, lensing, Doppler beaming and Rømer delay, are not detectable in our light curves. The irradiation is approximated by assigning a new temperature to the heated side of the companion:

$$\sigma T_{\text{sec}}'^4 = \sigma T_{\text{sec}}^4 + F_{\text{irr}} = \sigma T_{\text{sec}}^4 \left[1 + \alpha \left(\frac{T_{\text{prim}}}{T_{\text{sec}}} \right)^4 \left(\frac{R_{\text{prim}}}{a} \right)^2 \right]$$

with α being the Bond albedo of the companion and F_{irr} the irradiating flux, accounting for the angle of incidence

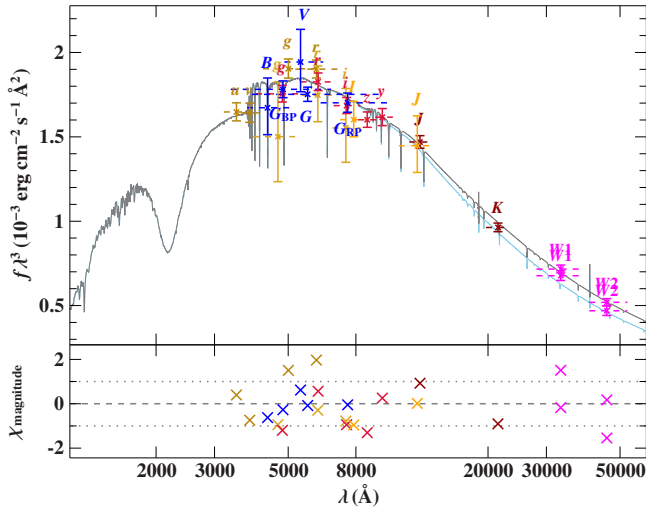


Figure 7. Comparison of synthetic and observed photometry (flux times wavelength to the power of three): *Top panel:* SED, filter-averaged fluxes converted from observed magnitudes. Dashed horizontal lines depict the approximate width of the respective filters (widths at tenth maximum). The best-fitting model, smoothed to a spectral resolution of 6 \AA , is shown in gray. *Bottom panel:* residual χ , difference between synthetic and observed magnitudes divided by the corresponding uncertainties. The different photometric systems are assigned the following colours: SDSS (APASS, golden; Alam et al. 2015); SkyMapper (golden; Wolf et al. 2018; Onken et al. 2019); PAN-STARRS (red; Chambers & et al. 2017); Johnson (APASS, blue; Henden et al. 2015); Gaia (blue; Evans et al. 2018 with corrections and calibrations from Maíz Apellániz & Weiler 2018); DENIS (yellow; Fouqué et al. 2000); VHS-DR6 (brown; Lawrence et al. 2007); WISE (magenta; Cutri & et al. 2014; Schlafly et al. 2019).

and distance from the hot subdwarf. If the irradiation effect is very strong, the description given above might not be sufficient. The backside of the irradiated star is completely unaffected in this description, but heat transport could heat it up, increasing the luminosity of unirradiated parts as well.

Since the model contains many parameters, not all of them independent, we fixed as many parameters as possible (see Table 4). The sDOB temperature was fixed to the temperature determined from the spectroscopic fit. The gravitational darkening coefficients were fixed to the values expected for a radiative atmosphere for the primary (von Zeipel 1924) and a convective atmosphere for the secondary (Lucy 1967), using a black-body approximation to calculate the resulting intensities. More sophisticated models such as those proposed by Espinosa Lara & Rieutord (2011) or Claret & Bloemen (2011, see also Claret et al. 2020) were not used because the deformations from a spherical shape are very small and in fact gravity darkening has almost no impact. For the limb darkening of the primary, we adopted a quadratic limb darkening law using the tables by Claret & Bloemen (2011). As the tables include only surface gravities up to $\log g = 5$, we used the values closest to the parameters derived by the spectroscopic analysis. As the two stars are almost spherical (we do not see significant ellipsoidal deformations), the light curve is not sensitive to the mass ratio and therefore we computed solutions with different, fixed mass ratios. To localize the best set of parameters, we used

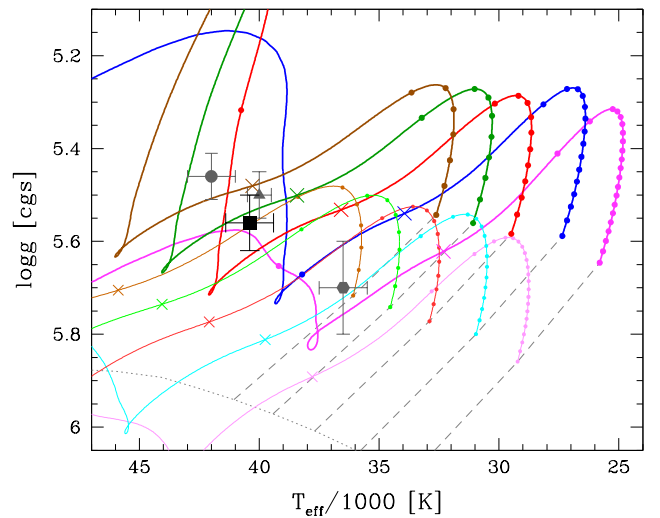


Figure 8. $T_{\text{eff}}\text{-}\log g$ diagram with the position of EPIC 216747137 (square symbol) compared with the evolutionary tracks by Han et al. (2002) for different stellar masses: from right to left 0.45 , 0.50 , 0.55 , 0.60 and $0.65 M_{\odot}$, (magenta, blue, red, green and brown respectively in the online version). The envelope mass is $0.005 M_{\odot}$ (thick lines) or 0.001 (thin lines and light colours). Along the evolutionary tracks, the age differences between adjacent dots are 10^7 years. The crosses mark the point of central helium exhaustion. Helium main sequence and zero-age EHB (ZAEHB) are shown as dotted and dashed lines respectively. The positions of the evolved HW Vir systems AA Dor (circle, Klepp & Rauch 2011) and V1828 Aql (triangle, Almeida et al. 2012) and of the evolved reflection-effect sdB+dM binary HS 2333+3927 (pentagon, Heber et al. 2004) are also reported. Note that AA Dor and V1828 Aql have masses of 0.47 and $0.42 M_{\odot}$ respectively, and therefore should definitely be post-EHB (compare with the $0.45 M_{\odot}$ (magenta) and $0.50 M_{\odot}$ (blue) tracks).

a SIMPLEX algorithm (Press et al. 1992) varying the inclination, the radii, the temperature of the companion, the geometric albedo of the companion (A_2), the limb darkening of the companion, the period and the time of the primary eclipse. Moreover, we also allowed for corrections of a linear trend, which is often absorbed in observing hot stars, as the comparison stars are often redder and so the correction for the air mass is often insufficient (slope). The model of the best fit is shown in Fig. 9, together with the observations and the residuals.

To get an idea about the degeneracy of the light curve solutions, as well as the errors of the parameters, we performed also Markov-Chain Monte-Carlo (MCMC) computations using the best solution obtained with the SIMPLEX algorithm as a starting value and varying the radii, the inclination, the temperature of the companion, as well as the albedo of the companion (Fig. A1,A2,A3). A clear correlation between the radius of the companion, the inclination, and the geometric albedo of the companion (A_2) can be seen, which results from the fact that the companion is only visible in the light curve due to the reflection effect and the amplitude depends on the inclination, the radius of the companion and the albedo, as well as the separation and temperature and radius of the primary, which is given by the spectroscopic analysis.

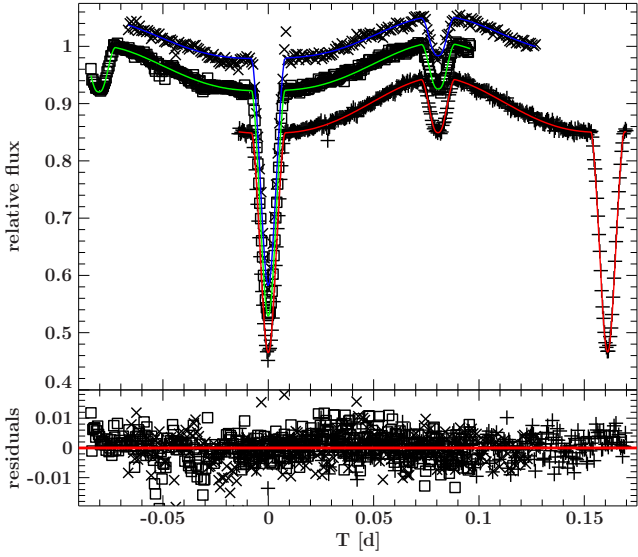


Figure 9. Normalized SAAO B(\times), V(\square) and R($+$)-band light curves together with the best fit. For better visualisation the V and R band light curves have been shifted. The lower panel shows the residuals.

Table 4. Parameters of the light curve fit of the SAAO BVR-band light curves for the best model.

band	B	V	R
Fixed Parameters			
q		0.175	
P		0.1610732	
$T_{\text{eff, sdB}}$		40400	
$x_{1,1}$	0.0469	0.0434	0.0379
$x_{1,2}$	0.2668	0.2346	0.2082
g_1		0.25	
g_2		0.08	
Fitted parameters			
i	85.04 ± 0.40	85.62 ± 0.19	85.51 ± 0.14
r_1/a	0.1887 ± 0.0016	0.1890 ± 0.0008	0.1887 ± 0.0005
r_2/a	0.1251 ± 0.0028	0.1216 ± 0.0012	0.1222 ± 0.0009
$T_{\text{eff, comp}}$	3000 ± 500	2965 ± 482	3042 ± 503
A_2	0.95 ± 0.08	1.01 ± 0.04	1.25 ± 0.04
x_2	0.33	0.27	0.28
T_0	2457892.53884	2457891.57235	2457893.66629
slope	0.004729	0.003015	0.00088
$\frac{L_1}{L_1+L_2}$	0.98028	0.972691	0.94864

Table 5. Absolute parameters of the system

	best solution	post-EHB canonical
q	0.175	0.194
a [R_\odot]	1.121 ± 0.028	1.028 ± 0.025
M_{sdOB} [M_\odot]	0.620 ± 0.023	0.470 ± 0.017
M_{comp} [M_\odot]	0.109 ± 0.004	0.091 ± 0.003
R_{sdOB} [R_\odot]	0.212 ± 0.005	0.194 ± 0.005
R_{comp} [R_\odot]	0.137 ± 0.003	0.125 ± 0.003
$\log g_{\text{phot}}$ [cgs]	5.58 ± 0.01	5.54 ± 0.01

8 NATURE OF THE COMPANION

As stated before, it is not possible to derive the mass ratio from the light-curve analysis. Since we have only a single-lined system, it is necessary to look for other possibilities to constrain the mass ratio of the system. Taking into account the sdOB atmospheric parameters obtained from our spectroscopic analysis, the sdOB star is likely an evolved post-EHB star or just at the end of helium burning, depending on the hot subdwarf mass and envelope mass.

When we combine the analysis of the radial velocity curve and the light curve, we get different masses and radii of both components, as well as a different separation for each solution with a different mass ratio. From the spectroscopic analysis we derived the surface gravity of the hot subdwarf, which can be compared to a photometric surface gravity calculated from the mass and radius derived from the light-curve analysis and the mass function. Moreover, from the radius determined by the Gaia parallax and the SED fit, we can calculate a Gaia surface gravity. The comparison of the photometric, spectroscopic, and Gaia surface gravity is shown in Fig. 10. An agreement is seen for a mass between ~ 0.47 and $\sim 0.67 M_\odot$. This means a post-EHB hot subdwarf with a canonical mass of $0.47 M_\odot$ cannot be excluded.

Another possibility to constrain the masses further is to consider the mass-radius relation of the companion (Fig. 11), and compare it to theoretical predictions (Baraffe et al. 2003; Chabrier & Baraffe 1997). Using the mass-radius relation for the cool companion, the best agreement is found for a sdOB mass of $\sim 0.62 M_\odot$. This is hence the most consistent solution, that implies a $\sim 2\%$ inflation of the M-dwarf radius. A lower mass would imply a more inflated radius for the M dwarf.

In Table 5 we consider two solutions (absolute system parameters) of the light curve analysis resulting from two different assumptions on the mass ratio q . A massive one at $q=0.175$, corresponding to an sdOB mass of $0.62 M_\odot$, which we prefer because it avoids strong inflation of the companion, and a second solution at $q=0.194$, which corresponds to the canonical mass ($M=0.47 M_\odot$). For the preferred solution of a high mass post-EHB star, we obtain a companion mass of $0.109 \pm 0.004 M_\odot$, corresponding to a low-mass M-dwarf. For a canonical mass sdOB, the mass of the M star would be even less ($0.091 \pm 0.003 M_\odot$), only slightly above the stellar mass limit.

9 SUMMARY AND DISCUSSION

EPIC 216747137 is a new HW Vir system that belongs to the small subgroup of eclipsing hot subdwarf binaries in which the primary is a hot, evolved, sdOB star. The other two members of this group, AA Dor and V1828 Aql, with a mass of 0.47 and $0.42 M_\odot$ respectively (Klepp & Rauch 2011; Almeida et al. 2012), should definitely be post-EHB stars (and this is particularly true for AA Dor that has been intensively studied by various teams). While for EPIC 216747137, due to its larger mass of ~ 0.62 , we can just say that it is close, and likely beyond, central helium exhaustion.

Among the 20 published HW Vir systems, only AA Dor, V1828 Aql and EPIC 216747137 have effective temperatures near 40 kK, while all the others have T_{eff} between 25 and

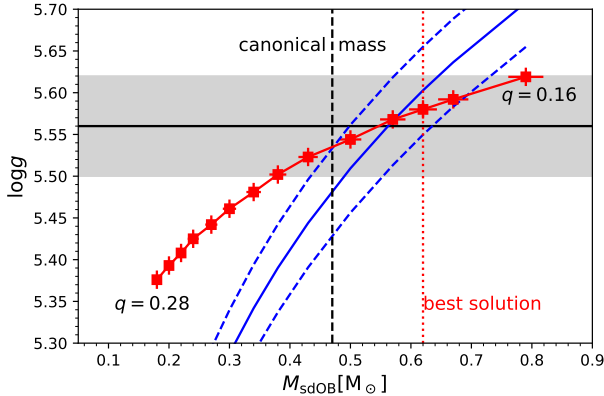


Figure 10. Mass of the sdOB versus the photometric $\log g$ for different mass ratios from 0.16 to 0.28 in steps of 0.1 (adding 0.175 for the best solution). They were derived from combining the results from the analysis of the light curve and radial velocity curve. The grey area marks the spectroscopic $\log g$ that was derived by the spectroscopic analysis. The blue lines mark the surface gravity derived from the radius determined by the Gaia parallax and the SED fit. The vertical lines represent the two solutions which are given in Table 5.

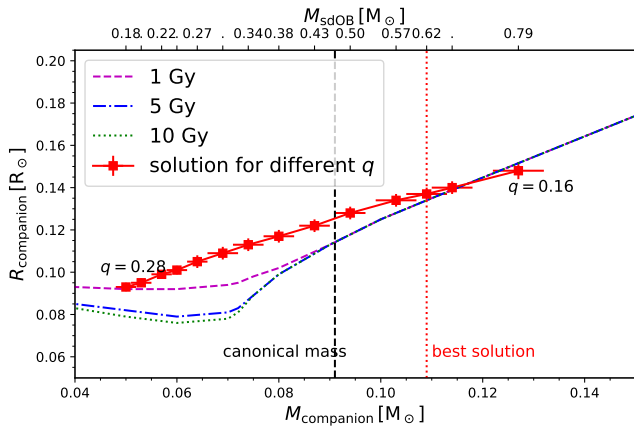


Figure 11. Comparison of theoretical mass-radius relations of brown dwarfs by Baraffe et al. (2003) and low-mass M dwarfs by Chabrier & Baraffe (1997) for an age of 1 Gyr (dashed), 5 Gyr (dotted-dashed) and 10 Gyr (dotted) to results from the light curve analysis. Each error cross represents a solution from the light curve analysis for a different mass ratio ($q = 0.16 - 0.28$ in steps of 0.1 and adding 0.175 for the best solution). The vertical lines represent the two solutions of Table 5.

35 kK, compatible with He-core burning (Wolz et al. 2018). Moreover, these three hotter HW Vir systems seem to follow a different relation in the $T_{\text{eff}}\text{-}\log y$ plane (Edelmann et al. 2003) respect to all the other HW Vir stars. The position of all the published HW Vir in a $T_{\text{eff}}\text{-}\log y$ plane can be seen in Wolz et al. (2018, Fig. 5). Since the number of new HW Vir systems is rapidly increasing, with 25 new systems already spectroscopically confirmed and many more to come (Schaffenroth et al. 2019), the larger statistics will allow us to confirm or not that HW Vir stars follow two different sequences in the $T_{\text{eff}}\text{-}\log y$ plane.

The orbital period of EPIC 216747137, ~ 0.161 days, and the mass of its dM companion, $\sim 0.11 M_{\odot}$, fit well with the period distribution and the companion mass distribution of the hot subdwarf binaries with a dM companion (Kupfer et al. 2015, Fig. 7 and 8). However, in the preferred light curve solution, the sdOB mass is unusually high ($0.62 M_{\odot}$). Such a high mass could result from post-AGB evolution, but this possibility is ruled out because it would imply a luminosity ten times higher than observed. When we consider constraints from spectroscopy, light curve solution and parallax, the mass must be between 0.47 and $0.67 M_{\odot}$. Hence a mass as low as $0.47 M_{\odot}$ can not be ruled out, but it implies that the cool companion is significantly inflated. Although inflation in M dwarfs is not a well understood phenomenon (see e.g. Parsons et al. 2018), a strong inflation appears quite unlikely, and this is why we prefer the high-mass option.

A mass as high as $\sim 0.62 M_{\odot}$ provides a challenge for the hot subdwarf formation theories since the CE ejection channel struggles to form stars with a mass higher than ~ 0.47 , while the RLOF channel does not work for orbital periods shorter than ~ 1 day (see e.g. Han et al. 2003, Fig. 12 and 10 respectively).

Another interesting aspect of our results is that EPIC 216747137 is not synchronized. Among the other 9 systems with published rotational velocities, only three of them are not synchronised (Schaffenroth et al. 2020, submitted, and references therein), all of them being relatively young and not evolved (and with a BD candidate companion, but this might be related to a selection effect considering that it is easier to obtain high-resolution data when the companion is a BD), while the other six more evolved systems are all synchronised. The growing number of synchronized systems seems in contradiction with the prediction by Preece et al. (2018) that synchronization time-scales are longer than the sdB lifetime.

Hot subdwarf stars are found in all stellar populations (Martin et al. 2017; Luo et al. 2020). EPIC 216747137 lies just 155 pc below the Galactic plane. This hints at thin disc membership. In order to check this assumption, we carried out a kinematical investigation calculating Galactic trajectories in a Galactic potential (for details see appendix B). The Galactic orbit is almost perfectly circular and the binary orbits within (though close to) the solar circle (Fig. B1). Hence, we conclude that the binary belongs to the thin disc population, which is also confirmed by its position in the Toomre diagram (Fig. B2).

ACKNOWLEDGEMENTS

The *K2* data presented in this paper was obtained from the Mikulski Archive for Space Telescopes (MAST). Space Telescope Science Institute is operated by the Association of Universities for Research in Astronomy, Inc., under NASA contract NAS5-26555. This paper uses observations made at the South African Astronomical Observatory (SAAO). The spectroscopic results are based on observations collected at the MPG/ESO 2.2 m telescope; at the 2.6 m Nordic Optical Telescope (NOT), operated jointly by Denmark, Finland, Iceland, Norway, and Sweden; and at the 6.5 m Magellan I telescope. RS acknowledges financial support from the INAF project on “Stellar evolution and asteroseismology in

the context of the PLATO space mission” (PI S. Cassisi). VS is supported by the Deutsche Forschungsgemeinschaft, DFG through grant GE 2506/9-1. DK thanks the University of the Western Cape and the National Research Foundation of South Africa for financial support. We thank Jantje Freudenthal for support at the SAAO 1m Elizabeth telescope, Michel Rieutord and an anonymous referee for useful comments. RS wishes to remember and thank Nicolò D’Amico, President of INAF, who suddenly passed away a few days before the submission of this article.

DATA AVAILABILITY

The data underlying this article will be shared on reasonable request to the corresponding author.

REFERENCES

- Alam S., et al., 2015, *ApJS*, **219**, 12
- Allen C., Santillan A., 1991, *Rev. Mex. Astron. Astrofis.*, **22**, 255
- Almeida L. A., Jablonski F., Tello J., Rodrigues C. V., 2012, *MNRAS*, **423**, 478
- Auer L. H., Mihalas D., 1972, *ApJS*, **24**, 193
- Bailer-Jones C. A. L., Rybizki J., Fousneau M., Mantelet G., Andrae R., 2018, *AJ*, **156**, 58
- Baraffe I., Chabrier G., Barman T. S., Allard F., Hauschildt P. H., 2003, *A&A*, **402**, 701
- Baran A. S., Bachulski S., Curyło M., 2016, *IAU Focus Meeting*, **29B**, 497
- Beauchamp A., Wesemael F., Bergeron P., 1997, *ApJS*, **108**, 559
- Brahm R., Jordán A., Espinoza N., 2017, *PASP*, **129**, 034002
- Chabrier G., Baraffe I., 1997, *A&A*, **327**, 1039
- Chambers K. C., et al. 2017, *VizieR Online Data Catalog*, p. II/349
- Charpinet S., et al., 2011, *Nature*, **480**, 496
- Charpinet S., Giammichele N., Zong W., Van Grootel V., Brassard P., Fontaine G., 2018, *Open Astronomy*, **27**, 112
- Claret A., Bloemen S., 2011, *A&A*, **529**, A75
- Claret A., Cukanovaite E., Burdge K., Tremblay P. E., Parsons S., Marsh T. R., 2020, *A&A*, **634**, A93
- Clausen D., Wade R. A., 2011, *ApJ*, **733**, L42
- Clausen D., Wade R. A., Kopparapu R. K., O’Shaughnessy R., 2012, *ApJ*, **746**, 186
- Copperwheat C. M., Marsh T. R., Dhillon V. S., Littlefair S. P., Hickman R., Gänsicke B. T., Southworth J., 2010, *MNRAS*, **402**, 1824
- Cutri R. M., et al. 2014, *VizieR Online Data Catalog*, p. II/328
- Drechsel H., et al., 2001, *A&A*, **379**, 893
- Eastman J., Siverd R., Gaudi B. S., 2010, *PASP*, **122**, 935
- Edelmann H., Heber U., Hagen H. J., Lemke M., Dreizler S., Napiwotzki R., Engels D., 2003, *A&A*, **400**, 939
- Espinosa Lara F., Rieutord M., 2011, *A&A*, **533**, A43
- Evans D. W., et al., 2018, *A&A*, **616**, A4
- Fitzpatrick E. L., Massa D., Gordon K. D., Bohlin R., Clayton G. C., 2019, *ApJ*, **886**, 108
- Fontaine G., Brassard P., Charpinet S., Green E. M., Randall S. K., Van Grootel V., 2012, *A&A*, **539**, A12
- Fouqué P., et al., 2000, *A&AS*, **141**, 313
- Fuhrmann K., 2004, *Astronomische Nachrichten*, **325**, 3
- Geier S., et al., 2011, *ApJ*, **731**, L22
- Giddings J. R., 1981, PhD thesis, Univ. London
- Han Z., Podsiadlowski P., Maxted P. F. L., Marsh T. R., Ivanova N., 2002, *MNRAS*, **336**, 449
- Han Z., Podsiadlowski P., Maxted P. F. L., Marsh T. R., 2003, *MNRAS*, **341**, 669
- Han Z., Chen X., Lei Z., Podsiadlowski P., 2012, *ASP Conference Series*, **452**, 3
- Heber U., 2016, *PASP*, **128**, 966
- Heber U., et al., 2004, *A&A*, **420**, 251
- Heber U., Irrgang A., Schaffenroth J., 2018, *Open Astronomy*, **27**, 35
- Henden A. A., Levine S., Terrell D., Welch D. L., 2015, in *American Astronomical Society Meeting Abstracts #225*. p. 336.16
- Hirsch H. A., 2009, PhD thesis, Friedrich-Alexander University Erlangen-Nürnberg
- Hubeny I., Hummer D. G., Lanz T., 1994, *A&A*, **282**, 151
- Irrgang A., Wilcox B., Tucker E., Schiefelbein L., 2013, *A&A*, **549**, A137
- Irrgang A., Kreuzer S., Heber U., Brown W., 2018, *A&A*, **615**, L5
- Kelson D. D., 2003, *PASP*, **115**, 688
- Kelson D. D., Illingworth G. D., van Dokkum P. G., Franx M., 2000, *ApJ*, **531**, 159
- Klepp S., Rauch T., 2011, *A&A*, **531**, L7
- Kramer M., Schneider F. R. N., Ohlmann S. T., Geier S., Schaffenroth V., Pakmor R., Roepke F. K., 2020, *arXiv e-prints*, p. [arXiv:2007.00019](https://arxiv.org/abs/2007.00019)
- Kupfer T., et al., 2015, *A&A*, **576**, A44
- Kupfer T., et al., 2020, *ApJ*, **891**, 45
- Kurucz R. L., 1996, in *Adelman S. J., Kupka F., Weiss W. W., eds, Astronomical Society of the Pacific Conference Series Vol. 108, M.A.S.S., Model Atmospheres and Spectrum Synthesis*. p. 160
- Lawrence A., et al., 2007, *MNRAS*, **379**, 1599
- Lindegren L., et al., 2018, *A&A*, **616**, A2
- Lucy L. B., 1967, *Z. Astrophys.*, **65**, 89
- Luo Y., Németh P., Li Q., 2020, *ApJ*, **898**, 64
- Maíz Apellániz J., Weiler M., 2018, *A&A*, **619**, A180
- Martin P., Jeffery C. S., Naslim N., Woolf V. M., 2017, *MNRAS*, **467**, 68
- Maxted P. F. L., Heber U., Marsh T. R., North R. C., 2001, *MNRAS*, **326**, 1391
- Napiwotzki R., Green P. J., Saffer R. A., 1999, *ApJ*, **517**, 399
- Napiwotzki R., Karl C. A., Lisker T., Heber U., Christlieb N., Reimers D., Nelemans G., Homeier D., 2004, *Ap&SS*, **291**, 321
- Onken C. A., et al., 2019, *Publ. Astron. Soc. Australia*, **36**, e033
- Parsons S. G., Marsh T. R., Copperwheat C. M., Dhillon V. S., Littlefair S. P., Gänsicke B. T., Hickman R., 2010, *MNRAS*, **402**, 2591
- Parsons S. G., et al., 2018, *MNRAS*, **481**, 1083
- Pauli E. M., Napiwotzki R., Heber U., Altmann M., Odenkirchen M., 2006, *A&A*, **447**, 173
- Pelisolì I., Vos J., Geier S., Schaffenroth V., Baran A. S., 2020, *arXiv e-prints*, p. [arXiv:2008.07522](https://arxiv.org/abs/2008.07522)
- Preece H. P., Tout C. A., Jeffery C. S., 2018, *MNRAS*, **481**, 715
- Press W. H., Teukolsky S. A., Vetterling W. T., Flannery B. P., 1992, *Numerical recipes in FORTRAN. The art of scientific computing*
- Ratzloff J. K., et al., 2020, *ApJ*, **890**, 126
- Reed M. D., et al., 2018, *Open Astronomy*, **27**, 157
- Saffer R. A., Bergeron P., Koester D., Liebert J., 1994, *ApJ*, **432**, 351
- Schaffenroth V., Geier S., Heber U., Kupfer T., Ziegerer E., Heuser C., Classen L., Cordes O., 2014, *A&A*, **564**, A98
- Schaffenroth V., Barlow B. N., Drechsel H., Dunlap B. H., 2015, *A&A*, **576**, A123
- Schaffenroth V., et al., 2019, *A&A*, **630**, A80
- Schaffenroth et al. 2020, *MNRAS*, submitted
- Schechter P. L., Mateo M., Saha A., 1993, *PASP*, **105**, 1342
- Schlafly E. F., Finkbeiner D. P., 2011, *ApJ*, **737**, 103
- Schlafly E. F., Meisner A. M., Green G. M., 2019, *ApJS*, **240**, 30
- Schlegel D. J., Finkbeiner D. P., Davis M., 1998, *ApJ*, **500**, 525
- Silvotti R., et al., 2014, *A&A*, **570**, A130

- Silvotti R., Østensen R. H., Telting J. H., 2020, arXiv e-prints, p. [arXiv:2002.04545](#)
- Soker N., 1998, *AJ*, **116**, 1308
- Stark M. A., Wade R. A., 2003, *AJ*, **126**, 1455
- Telting J., Østensen R., Reed M., Kjaerød F., Farris L., Baran A., Oreiro R., O'Toole S., 2014, ASP Conf. Series, **481**, 287
- Tremblay P. E., Bergeron P., 2009, *ApJ*, **696**, 1755
- Wolf C., et al., 2018, *Publ. Astron. Soc. Australia*, **35**, e010
- Wolz M., et al., 2018, *Open Astronomy*, **27**, 80
- Wood J. H., Saffer R., 1999, *MNRAS*, **305**, 820
- von Zeipel H., 1924, *MNRAS*, **84**, 665

APPENDIX A: MCMC FITS OF THE SAAO BVR LIGHT CURVES

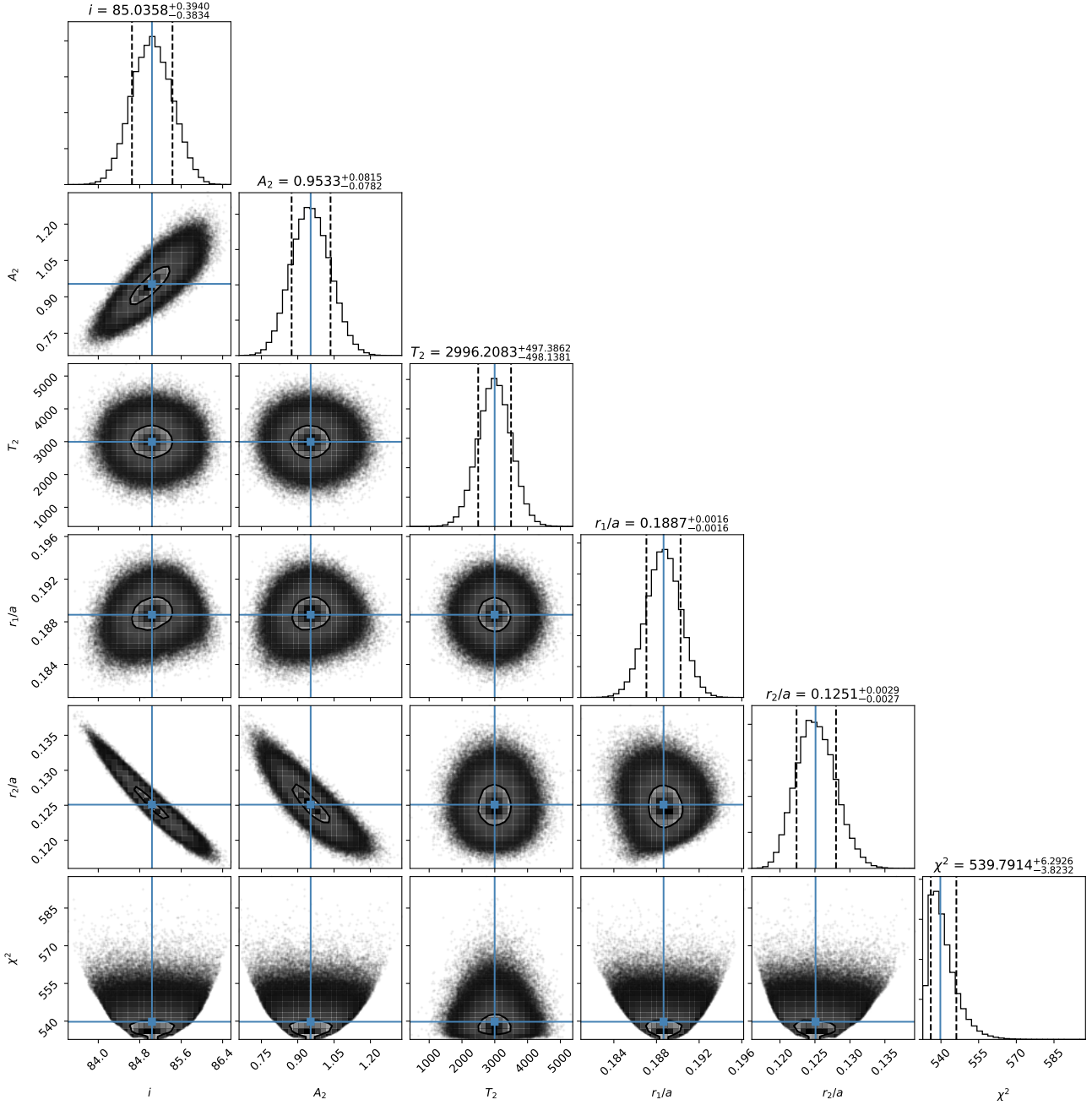


Figure A1. MCMC computations showing the degeneracy and the parameter errors of the B-band light curve solutions.

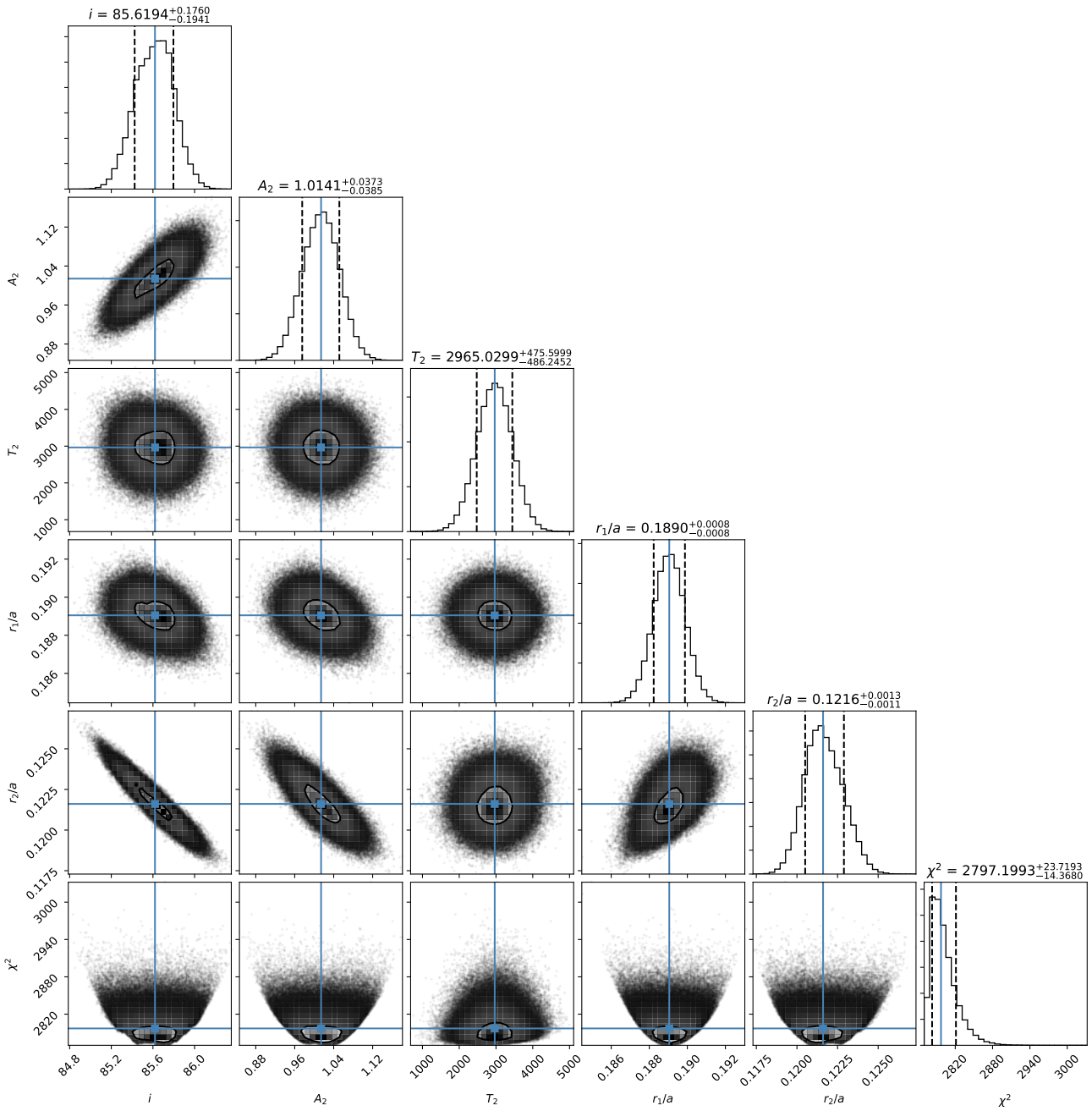


Figure A2. Same as Fig. A1 but for the V-band light curve.

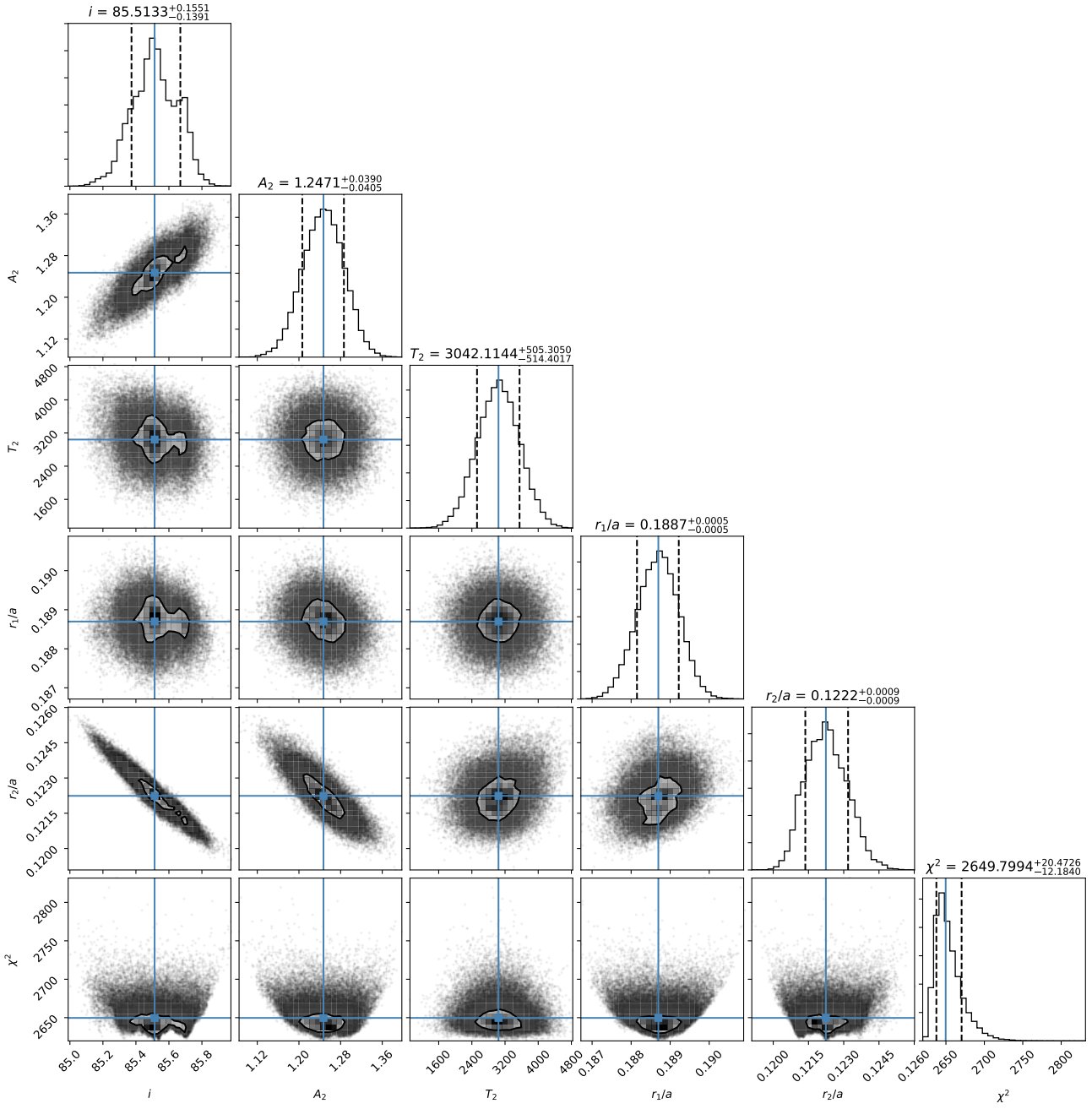


Figure A3. Same as Fig. A1 but for the R-band light curve.

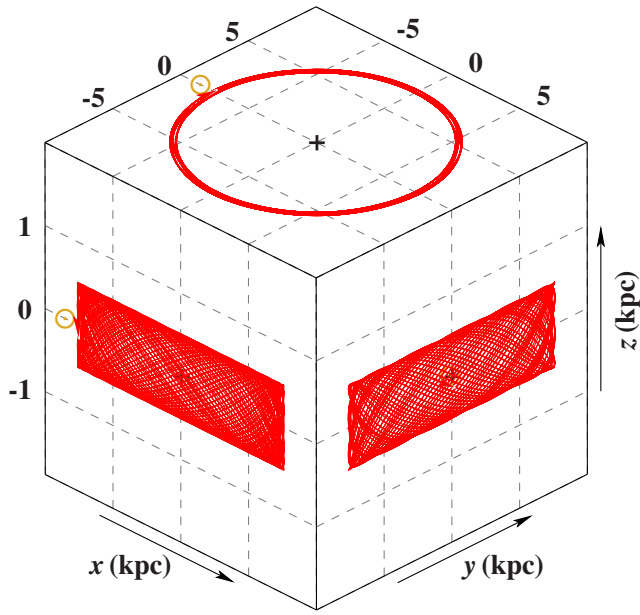


Figure B1. EPIC 216747137's three-dimensional orbit in a Cartesian Galactic coordinate system. The centre of the Galaxy lies at the origin, the Sun (yellow circled dot) on the negative x-axis. The z-axis points to the Galactic north pole. Trajectories were computed back in time for 10 Gyrs using a standard, axisymmetric model for the Galactic gravitational potential (an updated version of that of [Allen & Santillan \(1991\)](#), see [Irrgang et al. 2013](#), for details). The shape of the orbit is almost circular, with vertical oscillations of a few hundred pc amplitude, typical for a thin-disk star (see e.g. [Pauli et al. 2006](#)).

APPENDIX B: KINEMATICS OF EPIC 216747137

This paper has been typeset from a $\text{\TeX}/\text{\LaTeX}$ file prepared by the author.

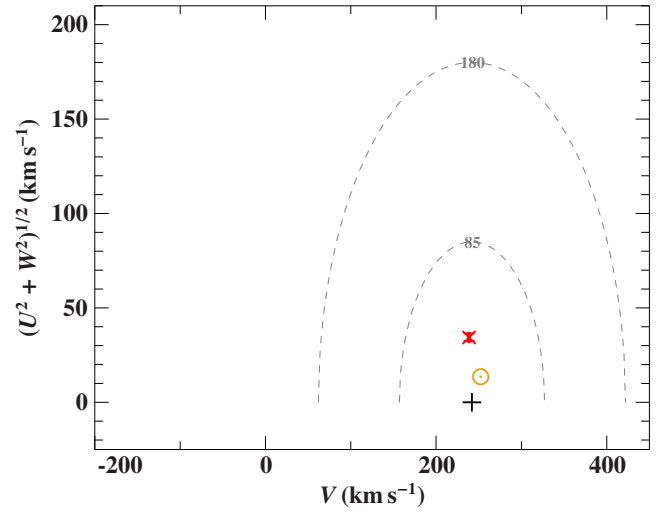


Figure B2. The position of EPIC 216747137 (red cross with 1σ error bars) in the Toomre diagram. The velocity component V is measured in the direction of the rotation of the Galaxy, U towards the Galactic centre, and W perpendicular to the plane. The yellow circled dot marks the position of the Sun. The local standard of rest (LSR) is marked by a plus sign. According to [Fuhrmann \(2004\)](#), the boundaries for thin and thick disk are located at 85 km s^{-1} and 180 km s^{-1} respectively (dashed circles centered around the LSR).